

UNIVERSITY OF LATVIA



Jānis Šmits

# Microscale measurements with nitrogen-vacancy centers in diamond

SUMMARY OF DOCTORAL THESIS

Submitted for the degree of Doctor of physics, mechanics and astronomy  
Subfield: Laser physics and spectroscopy

Riga, 2020

The doctoral thesis was carried out at the Chair of Physics  
Faculty of Physics, Mathematics and Optometry, University of Latvia from 2017 to 2020

The thesis contains the introduction, 4 chapters, a reference list and no appendices  
Form of the thesis: dissertation in Physics Astronomy and Mechanics, subfield: laser physics and spectroscopy  
Supervisor: Dr. Florian Gahbauer

Reviewers:

- 1) *Prof. Uldis Rogulis, senior researcher at the University of Latvia Institute of Solid state Physics*
- 2) *Dr. Kristaps Jaudzems, senior researcher at the Latvia Organic Synthesis Institute*
- 3) *Dr. Audrius Alkauskas, head of the Electronic Structure Theory laboratory at the Center for Physical Sciences and Technology, Vilnius.*

The thesis will be defended at a public online session of the Doctoral Committee of Physics, Astronomy and Mechanics,  
University of Latvia on June 16th

---

The thesis is available at the Library of the University of Latvia, Kalpaka blvd. 4.

Chairman of the Doctoral Committee: Ruvins Ferbers \_\_\_\_\_  
(paraksts)

Secretary of the Doctoral Committee: Karlīna Engere \_\_\_\_\_  
(paraksts)

# Abstract

The negatively charged nitrogen-vacancy (NV) center in diamond possesses excellent room-temperature coherence properties and is a very promising candidate platform for the next generation of high sensitivity magnetic sensors. In this work we investigated the relaxation dynamics and sensing performance of the nitrogen-vacancy (NV) center.

while examining the NV concentration dependent population relaxation times  $T_1$  we found strong evidence of NV-NV dipole-dipole couplings being the dominant relaxation channel for high NV concentrations ( $>1$  ppm).

We also studied two distinct NV magnetometry modalities. One of them was the NV based magnetic microscope which was used to obtain optical resolution magnetic signals. Several key insights on experimental design were obtained from these efforts which, we believe, could enable us to study time-dependent magnetic processes.

The other was a high-sensitivity and high-spectral resolution NV based nuclear magnetic resonance spectrometer was built and the first two-dimensional NMR signal of an external analyte was obtained on such a system.

## List of papers used in the work and corresponding author contributions

A. Jarmola et al., “Longitudinal spin-relaxation in nitrogen-vacancy centers in electron irradiated diamond”, Applied Physics Letters **107**, 242403 (2015)

**Author’s contributions:** Performed data analysis, experimental measurements, participated in the construction of the experimental setup.

J. Smits et al., “Estimating the magnetic moment of microscopic magnetic sources from their magnetic field distribution in a layer of nitrogen-vacancy (NV) centres in diamond”, The European Physical Journal Applied Physics **73**, 20701 (2016)

**Author’s contributions:** Performed data analysis, developed the deconvolution and magnetic parameter fitting code

J. Smits et al., “Two-dimensional nuclear magnetic resonance spectroscopy with a microfluidic diamond quantum sensor”, Science Advances **5**, eaaw7895 (2019)

**Author’s contributions:** Performed data analysis, experimental measurements, setup construction, wrote control software

P. Kehayias et al., “Solution nuclear magnetic resonance spectroscopy on a nanostructured diamond chip”, Nature Communications **8**, 188 (2017)

**Author’s contributions:** Performed part of the data analysis, performed part of the experimental measurements

I. Fescenko et al., “Diamond magnetic microscopy of malarial hemozoin nanocrystals”, Physical Review Applied **11**, 034029 (2019)

**Author’s contributions:** Wrote part of the control software

# Contents

<b>1</b>	<b>Background</b>	<b>1</b>
1.1	The NV center structure . . . . .	2
1.2	Optically detected magnetic resonance of the NV center . .	5
<b>2</b>	<b>Characterization of relaxation rates in NV centers</b>	<b>10</b>
2.1	Experimental realization . . . . .	11
<b>3</b>	<b>Magnetic microscopy with NV centers</b>	<b>17</b>
3.1	Basic components and principles of operation of the dia- mond magnetic microscope . . . . .	18
3.2	Magnētisku daļiņu magnētiskā mikroskopija . . . . .	20
3.3	Magnetic imaging of malarial hemozoin . . . . .	25
<b>4</b>	<b>Nuclear magnetic resonance spectroscopy with NV centers</b>	<b>27</b>
4.1	NMR spectroscopy . . . . .	28
4.2	Statistiskās polarizācijas spektroskopija ar NV centriem . .	28
4.3	Microscale sensing of thermal polarization . . . . .	31
<b>5</b>	<b>Conclusions</b>	<b>36</b>
	<b>Bibliography</b>	<b>38</b>

# 1 Background

In recent years research of quantum technologies has progressed considerably with many research groups now focusing on not only fundamental research but concrete applications and product development [1–3]. The most widely known quantum technology is probably the quantum computer. Several public and private bodies (IBM, ETH-Zurich, Rigetti and Microsoft [4]) are offering development platforms and access to genuine quantum machines. In tandem with quantum computing the complementary field of quantum metrology has also experienced significant advances. While quantum computers seek to decouple the constituent qubits from the environment, quantum metrological devices exploit this coupling to probe the relevant environmental parameters. The most sensitive magnetometers, clocks, thermometers and other types of sensors rely on quantum effects enabling measurements at precision and scale inaccessible to classical analogues.

Quantum sensors can be realized in many different physical systems, among these is the the nitrogen-vacancy color center (NV center) in diamond which stands out with an array of remarkable properties. First, the ground spin state of the NV center can be both initialized and read out optically; in addition the spin state can be coherently manipulated using microwave radiation. Second, the spin coherence time ( $T_2$ ) even at room temperature can reach up to  $\sim$ ms [5] and reach seconds at liquid nitrogen temperatures [6]. Finally, the physically robust, chemically inert and bio-compatible diamond matrix hosting the defect possesses multiple excellent properties in the context of sensing. It is both physically and chemically robust and bio-compatible; it lends itself well to nanostructuring, which enables favorable geometries for sensing applications such as trenches [7] or nanopillars [8], and finally the potent fabrication processes familiar in the semiconductor industry such as chemical vapor deposition (CVD), delta-doping or ion implantation grant a high degree of control over the isotopical composition [5, 9, 10], NV concentration [11, 12] and spatial distribution [13, 14], which make it possible to tailor the quantum sensor to a particular application.

Samples of bulk NVs have managed to achieve a  $\sim \text{pT}/\sqrt{\text{Hz}}$  sensitivity [15] and microscale ensembles have reported a sensitivity as low as  $1.2 \text{ nT}/\mu\text{m}^{3/2}/\sqrt{\text{Hz}}$  [16]. While alternative platforms (alkali metal vapors or superconducting quantum interference devices) outperform the NV center in raw sensitivity they suffer from poor spatial resolution, higher technical complexity and operating temperatures incompatible with living organisms. This motivated me to set the following overall goal of the thesis: **Study the NV relaxation processes, build a NV based magnetic microscope and move the NV nuclear magnetic resonance spectrometer towards competitiveness with conventional techniques.**

To achieve this goal I set myself three tasks:

- Characterize the  $T_1$  relaxation rate as a function of NV concentration and use the data to infer the possible relaxation mechanisms.
- Construct a NV diamond magnetic microscope and evaluate the possibility of studying time-dependent processes with this technique.
- Examine the feasibility of performing two-dimensional nuclear magnetic resonance experiments with an NV based sensor.

The dissertation consists of four chapters the condensed versions of which make up this summary. Chapter one introduces the reader to the field of NV centers: the defects structure, characteristics and fabrication related questions. Chapter two explores the relaxation rate dependence on NV concentration. Chapter three reports on the development and optimization of an NV based magnetic microscope. Finally, chapter four describes the development and performance of an NV based NMR spectrometer.

The research on which the dissertation is based has been published in 5 peer-reviewed articles.

## The NV center structure

The nitrogen-vacancy center point defect in diamond with  $C_{3v}$  symmetry formed when a nitrogen atom replaces a carbon atom and, additionally, is joined by a vacancy in an adjacent carbon site, as shown in Fig. 1.1. There exist several charge state variations of the defect:  $\text{NV}^+$  [17, 18],  $\text{NV}^0$  [19] and  $\text{NV}^-$  [20–22] where the  $\text{NV}^0$  and  $\text{NV}^-$  are the predominant varieties [23]. The negatively charged center exhibits the properties that make it highly attractive. These properties are:

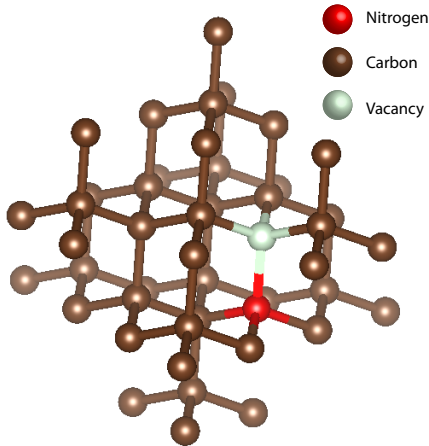


Figure 1.1: The structure of the NV center. For the negatively charged center the electron is mostly localized at the vacancy site. The axis connecting the nitrogen to the vacancy is the quantization axis.

- The spin state can be prepared optically.
- The spin state can be read out optically.
- Spin coherence times that are long compared to most other solid state qubit systems.

It is common in the literature to drop the “-“ sign, and this practice will also be employed in this work. It is thought that the source of the additional electron are substitutional nitrogen defects (also known as P1 centers) [20, 24]. The NV center itself possesses a  $C_{3v}$  symmetry with the symmetry axis aligned along the crystalline sites of the nitrogen and vacancy. In most bulk diamond/NV fabrication techniques all four possible alignment direction are equally probable resulting in four subsets of NV centers. However, preferential orientation along two directions can be achieved through clever substrate selection and appropriate CVD growth protocols [25, 26].

The general steps of fabricating a NV diamond are:

- Preparation of a diamond matrix with the necessary nitrogen,  $^{13}\text{C}$  content/volumetric distribution.
- Introduction of vacancy defects in the diamond either by ion or electron irradiation. In some cases the first and second steps are combined by using nitrogen as the vacancy forming ion. High-power

impulse lasers have also been used to both locally create vacancies and perform the annealing step to form NV centers [13, 27].

- High-temperature annealing in an oxygen-free atmosphere, which causes the vacancies to diffuse through the diamond until they encounter a site adjacent to a substitutional nitrogen.

There exist two main industrial processes that produce mono-crystalline diamond chips that are suitable for producing NV based sensors. The first is the high-pressure-high-temperature (HPHT) technique. At these environmental conditions graphite undergoes a phase transition to diamond. This is a relatively cheap process which produce stones with a relatively high nitrogen content (50 to 200 ppm are typical). The second method is chemical vapor deposition (CVD), where the diamond chip is fabricated by depositing carbon atoms layer by layer. This process is slower and more expensive, but yields chips with lower defect concentration. A type of diamond that is appearing more frequently in recently published research is the delta-doped CVD diamond [28–30]. With this technique nitrogen is introduced for a brief time during the growth process to create a spatially well defined distribution of nitrogen defects with a defined concentration. Another improvement in sensor quality can be obtained by using isotopically purified precursor gases. Around 1.1 % of natural abundance carbon is  $^{13}\text{C}$  which has a non-zero spin. The presence of this carbon isotope produces magnetic noise degrading sensor performance. By using pure  $^{12}\text{C}$  precursors it is possible to increase the coherence time of NV centers by eliminating  $^{13}\text{C}$  induced noise. [28–30].

The electronic energy structure and absorption/emission spectra in the triplet state manifold of the NV center are depicted in Fig. 1.2. The broad vibronic bands mean that excitation and emission can occur at different wavelengths, thus enabling easy separation between them by using dichroic mirrors or filters. Besides the direct optical transitions, there exists a nonradiative inter-system crossing to the metastable singlet state which can further transition back to the triplet through another radiation-free pathway. The fine structure spin Hamiltonian of the ground state triplet level  $^3\text{A}_2$  takes the form:

$$H_{gs} = D_{gs} (S_z^2 - S(S+1)/3) + \mu_B g \mathbf{S} \cdot \mathbf{B}, \quad (1.1)$$

, where  $D_{gs} = 2.87$  GHz is the ground state fine-structure splitting.  $\mu_B$  is the Bohr magneton,  $\mathbf{B}$  is the magnetic field vector. As was discussed in the introduction, the ground spin state can be both initialized and read out optically. The reason for this behavior can be understood by taking another look at the NV energy structure Fig. 1.3.

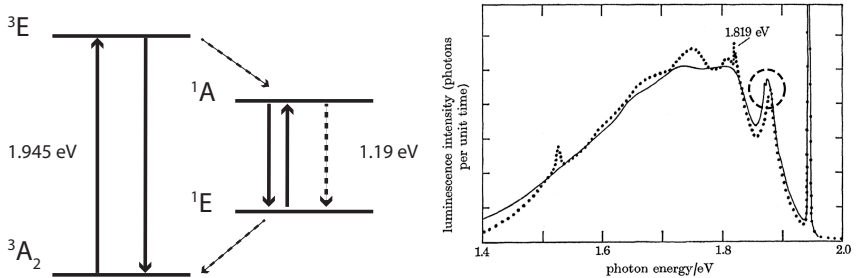


Figure 1.2: (Left) The electronic structure of the NV center. Solid arrows depict optical transitions and dashed arrows represent non-radiative transitions. The ground state is a spin triplet but it also has a metastable singlet state accessible from the excited  ${}^3E$  state. The states are named after the Mulliken symbols of the irreducible representation associated with the state. (Right) The emission (solid line) and absorption (dashed line, reflected along the zero-phonon line at 637 nm) spectra of the NV center [31].

The direct radiative relaxation is equally probable for all spin projections [32], however comparing the relative non-radiative relaxation rates of  $m_s = \pm 1$  and  $m_s = 0$  magnetic sublevels [33] yields a value of

$$\frac{\Gamma_0}{\Gamma_{\pm 1}} \approx 0.53, \quad (1.2)$$

indicating a strong preference of the  $m_s = \pm 1$  spin projection states to relax back to the ground state through the singlet system. The  ${}^1E \rightarrow {}^3A_2$  intersystem crossing exhibits only a weak spin projection dependence [34] resulting in optical pumping of the  $m_s = 0$  state. This phenomenon also accounts for the spin-projection-dependent fluorescence as the nonradiative channel competes with the radiative decay path. As a result the state with the lowest non-radiative relaxation contribution is the brightest.

## Optically detected magnetic resonance of the NV center

The simplest implementation of the NV center as a magnetic field sensor is optically detected magnetic resonance (ODMR) spectroscopy. The fluorescence intensity of the NVs is monitored as function of an applied microwave frequency. When on resonance, the microwaves induce transitions

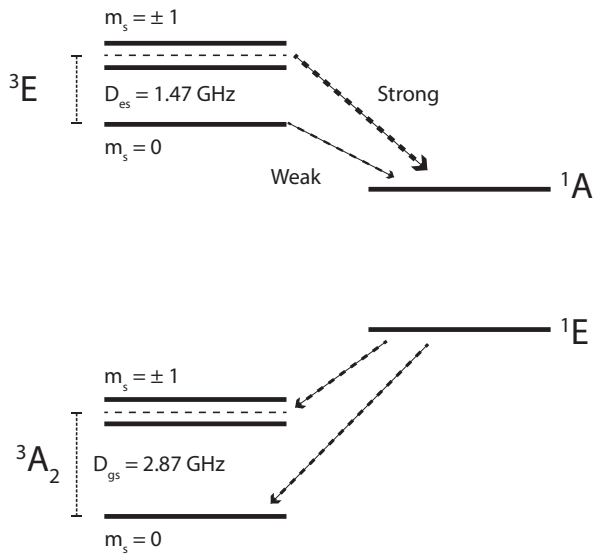


Figure 1.3: NV energy structure including the spin states. The excited state  $m_s = \pm 1$  spin projections have a high probability to perform an intersystem crossing to the singlet state while the transition back to the triplet state exhibits far less dependence on the spin projection.

between the  $m_s = 0$  and  $m_s = \pm 1$  spin states. As discussed in section 1.1 the  $m_s = \pm 1$  states exhibit a lower fluorescence level due to their higher probability of non-radiative decay allowing one to determine the energy difference between the two states. The levels are shifted (assuming all other external field, strain, and temperature variables are controlled for) according to the Zeeman term  $\mu_B g \mathbf{B} \cdot \mathbf{S}$  in Eq. 1.1. In almost all sensing applications the zero-field splitting  $D_{gs}$  is much larger than the magnitude of the magnetic field under investigation. This effectively means that only the axial component of the field is detected, as off-axis terms contribute to the energy splitting only in the second order. A typical experimental setup for ODMR detection is shown in Fig. 1.4(a). The diamond is optically excited in an epifluorescent configuration, where the excitation and fluorescence optical paths are partially overlapped. The observed ODMR spectrum depends on the angle between the NV center and the magnetic field. In the case depicted in Fig. 1.4(b) the magnetic field is aligned along one of the 4 possible NV axis. A symmetric resonance structure can be observed where the resonances at lower microwave frequencies correspond to  $m_s = 0 \rightarrow m_s = -1$  transitions and the ones at higher MW frequencies come from  $m_s = 0 \rightarrow m_s = +1$  transitions. The relative peak amplitudes (magnitude of the external field assumed  $\sim 200$  G or less) follow the relative concentrations of NV centers. There are three times as many NV centers which are at some angle relative to the magnetic field than those that are aligned with it which explains the 3:1 amplitude ratio.

It is possible to derive the transition frequency from the spectrum from which, in turn, it is possible to obtain the amplitude of the magnetic field. For example, if we consider the  $m_s = 0 \rightarrow m_s = +1$  transition the magnetic field amplitude can be expressed as:

$$B = \frac{\omega - D_{gs}}{\gamma}, \quad (1.3)$$

where  $\gamma \approx 2.8$  MHz/G is the electron gyromagnetic ratio. The sensitivity of an NV ODMR magnetometer  $\eta$  is determined by the signal contrast, fluorescence intensity (the photon shot noise is the fundamental limit in this experiment) and the resonance linewidth. The expression relating all of these quantities to the sensitivity is:

$$\eta \approx \mathcal{P}_{\mathcal{F}} \gamma \frac{\Delta\nu}{C\sqrt{R}}, \quad (1.4)$$

where  $\Delta\nu$  is the ODMR resonance linewidth,  $C$  is the contrast,  $R$  is the photon flux (number of detected photons per unit time) and  $\mathcal{P}_{\mathcal{F}}$  is a numerical constant ranging from 0.7 to 0.77 depending on the shape of the

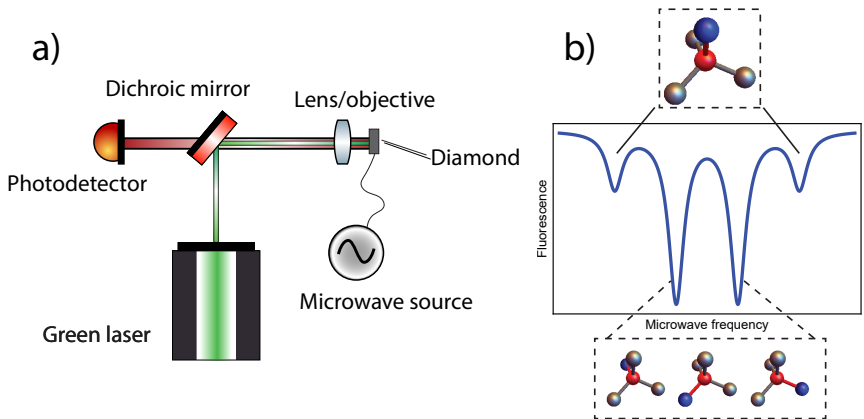


Figure 1.4: (a) A typical NV ODMR experimental setup. NV centers are excited with a green laser while microwaves are supplied through a wire or an antenna near the NV center. The excitation is focused and the fluorescence collected by the same optical element - usually a high numerical aperture objective. Any reflected green light is separated from the fluorescence by a dichroic mirror. After that the fluorescence is transformed into an electric signal by a photodiode. (b) An ODMR spectra in the case where an external field is aligned along one of the four possible NV orientations. The outermost peaks come from the aligned NVs while the inner ones correspond to one of the three possible orientations which are at an angle with respect to the applied magnetic field axis.

resonance (Gaussian or Lorentzian correspondingly). When performing ODMR experiments one needs to be careful when picking the microwave and optical powers. On one hand more power yields better fluorescence and higher contrast but on the other it leads to power broadening of the resonance [35]. When optimum conditions for both are met [15, 36] the magnetometer sensitivity can be expressed as:

$$\eta \approx \mathcal{P}_{\mathcal{F}} \gamma_{NV} \frac{1}{C \sqrt{RT_2^*}}, \quad (1.5)$$

where  $T_2^*$  is the ensemble decoherence time - the characteristic time in which information about the NV spin precession phase is lost (a more detailed discussion on this topic can be found in the dissertation itself). Pulsed techniques such as Ramsey, Hahn-echo, CPMG etc. have also been realized in NV centers demonstrating enhanced sensing performance under suitable circumstances. Regardless of the technique employed, longer coherence times lead to more sensitive detectors; it is also a parameter

that is strongly influenced by both the properties of the diamond and the environment in which the diamond is placed.

## 2 Characterization of relaxation rates in NV centers

The main factor impacting the coherence time of NV centers is its interaction with other paramagnetic defects in the diamond.

To discuss these interactions the NV community has adopted the language from the NMR field distinguishing two kinds processes.  $T_1$  describes the population (longitudinal) relaxation rate and  $T_2$  describes the coherence (transverse) relaxation rate. In literature sub- and super-scripted values are also often used ( $T_{1\rho}$ ,  $T_1^*$ ,  $T_2^*$  etc.) for effective relaxation time values that are different from the true relaxation times either due to the measurement process itself perturbing the spin system (such as an inversion recovery pulse introducing mixing effects in coupled systems [37]), inhomogeneous broadening caused by external field gradients or continuous driving fields applied to the spins.

In the previous chapter I mentioned that sophisticated CVD diamond synthesis techniques allow to significantly reduce the concentration of paramagnetic defects. One of the paramagnetic defects, that negatively impacts the sensor performance, is the P1 center: a substitutional nitrogen atom. Its' unpaired electron couples to the NV center through magnetic dipole-dipole interactions. On the other hand certain amount of nitrogen is necessary to form the NV centers in the first place, significantly decreasing the P1 concentration leads to lower defect density, lower fluorescence intensity and worse sensitivity (term  $R$  in equation (1.5)). These considerations mean that, in order to optimize the NV sensor performance, it is important to achieve high P1 to NV conversion efficiency.

The contributions to the effective relaxation time can be written as

[36]:

$$\begin{aligned} \frac{1}{T_2^*} = & \frac{1}{T_2^* \{\text{electronic spin bath}\}} + \frac{1}{T_2^* \{\text{nuclear spin bath}\}} + \\ & + \frac{1}{T_2^* \{\text{strain gradients}\}} + \frac{1}{T_2^* \{\text{electric field noise}\}} + \\ & + \frac{1}{T_2^* \{\text{magnetic field gradients}\}} + \frac{1}{T_2^* \{\text{temperature gradients}\}} + \\ & + \frac{1}{T_2^* \{\text{other}\}} + \frac{1}{2T_1}. \end{aligned}$$

Spatial inhomogeneities in extrinsic parameters such as magnetic/electric fields or temperature can be compensated for by appropriate experimental design. Intrinsic factors such as strain inhomogeneities or other paramagnetic defects can be addressed by optimum diamond synthesis conditions. Eventually the fundamental limiting coherence time limiting factor is the NV spin spin population relaxation time  $T_1$ . If the defect concentration is low at room temperature the population relaxation is mostly due to phonon processes [38, 39] but as the NV center concentration increases the NV-NV dipole-dipole couplings become more important. One of the experiments discussed in the dissertation investigated the NV center population relaxation dynamics as a function of NV concentration observing the transition from the phonon dominated to the dipole-dipole coupling dominated relaxation regimes.

## Experimental realization

To control for other external parameters such as paramagnetic impurity concentration we used a Schottky field emitter electron source from a TEM microscope to create vacancies in type 1b HPHT diamond with around around 200 ppm of substitutional nitrogen. 13 spots on the same chip were irradiated with different doses (same fluence) forming a layer between  $\sim 7 \mu\text{m}$  and  $\sim 20 \mu\text{m}$  thick.wo different approaches were used to estimate the vacancy distribution: a Monte-Carlo simulation using the CASINO software package [40] and from the total stopping power reported by ESTAR [41]. The results from the Monte-Carlo method are shown in Fig. 2.1.

After irradiation the sample was heated in a nitrogen atmosphere for three hours at  $800^\circ\text{C}$  to facilitate vacancy diffusion and capture by substitutional nitrogen defects to form NV centers. A wide-field fluorescence image of the irradiated spots is depicted in figure 2.2 and the corresponding

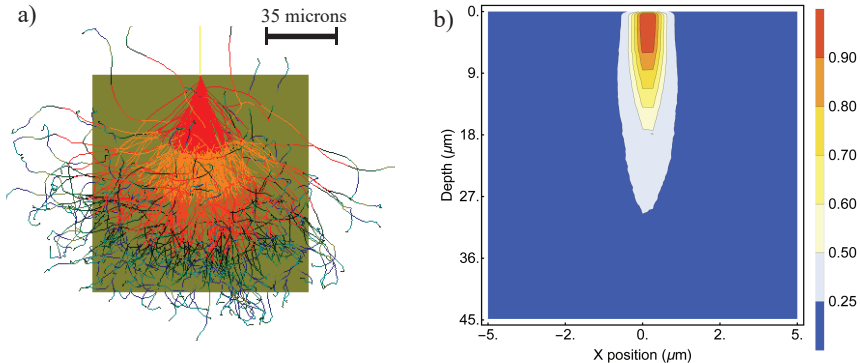


Figure 2.1: CASINO simulation of 200 keV electron beam impacting a  $100 \times 100 \times 100 \mu\text{m}$  diamond block. a) Trajectories of simulated electrons. Color scale represents the energy of the electron. b) Averaged normalized depth/energy distribution over 1000 simulated trajectories. Only electrons retaining at least 90% of their initial energy can displace carbon atoms and produce vacancies.

irradiation parameters are shown in table 2.1. The concentration estimates were obtained by assuming a linear fluorescence intensity/concentration dependence and scaling from a diamond with a known NV center concentration of 10 ppm.

The  $T_1$  relaxation measurement pulse sequence and a typical signal are shown in Fig. 2.3(a). It is a pulse experiment that begins by polarizing the NV centers in the  $m_s = 0$  state by laser illumination. The system is allowed to freely evolve for a time  $\tau$ . Finally another laser pulse is applied and the population distribution inferred from the observed fluorescence intensity. The NV center is initially in the  $m_s = 0$  state, then, as it is allowed to freely evolve it will approach thermodynamic equilibrium. At room temperature the energy splitting between the spin sublevels is much smaller than  $k_B T$  so at thermal equilibrium all spin projection components are populated with near equal probability. The system can alternatively be initialized in either of the  $m_s = \pm 1$  states by applying a resonant microwave  $\pi$  pulse shortly after the laser pulse. By subtracting the relaxation signals from the  $m_s = 0$  and either of the  $m_s = \pm 1$  states it is possible to cancel out the fluorescence from sources other than the aligned NVs (background fluorescence or the misaligned NV components). The relaxation rate  $T_1$  can be obtained by fitting the relaxation signal with a stretched exponential:

$$F(\tau) \sim e^{-(\tau/T_1)^\beta}, \quad (2.1)$$

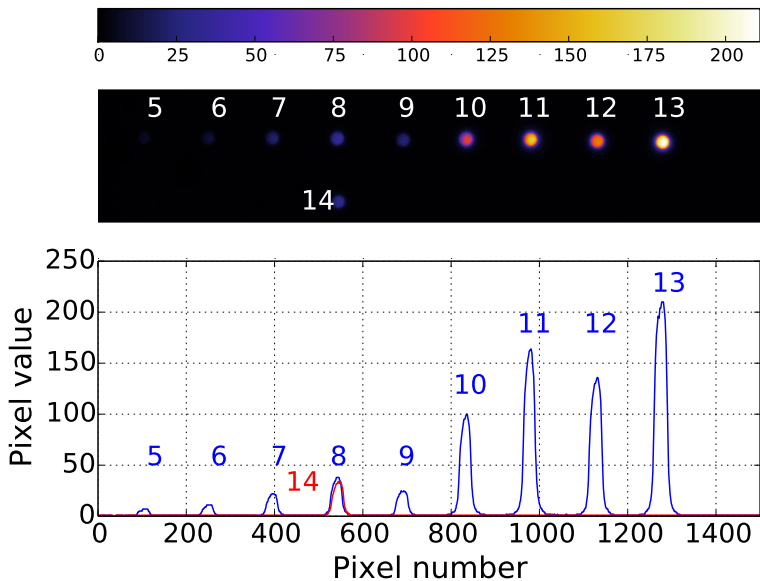


Figure 2.2: A fluorescence image of the irradiated spots on the diamond. The plot underneath the fluorescence image depicts the pixel value across a line-cut through all of the points.

where  $F(\tau)$  is the free evolution time  $\tau$  dependent fluorescence signal,  $T_1$  is the effective decay time and  $\beta$  is a coefficient describing the distribution of the relaxation rates. A lower value of  $\beta$  indicates a broader distribution. If the NV concentration is low  $\beta = 1$  and the individual relaxation time of each NV center is the same as the effective time  $T_1$ .

Fig. 2.3(b) depicts the experimental setup. The system consists of an epifluorescence microscope, already described in section 1.2. The diamond is placed at the center for three pairs of Helmholtz coils which control the magnetic field amplitude in the x, y and z directions. The laser is pulsed by an acousto-optic modulator and the microwaves are switched on and off by a solid-state switch. Both devices are controlled by a programmable TTL pulse generator with a 500 MHz clock frequency.

The Helmholtz enabled us to probe the  $T_1$  dependence on magnetic field. The NV spin sublevel energy changes with the applied magnetic field. In the case where the transition energy of two coupled defects matches they can exchange energy with a corresponding flip in the spin projection. In literature this is called flip-flop process as a spin flip in one defect induces

Spot Nr.	Integrated Fluorescence Intensity (arb. units)	Electron Dose (C/cm <sup>2</sup> )	Electron Flux (A/cm <sup>2</sup> )	Estimated NV <sup>-</sup> Concentration (ppm)
5	1400	1.76	$5.6 \times 10^{-2}$	0.2
6	2600	3.36	$5.6 \times 10^{-2}$	0.3
7	5700	6.72	$5.6 \times 10^{-2}$	0.7
8	10000	13.6	$5.6 \times 10^{-2}$	1.2
9	6300	27.2	$5.6 \times 10^{-2}$	0.7
10	29000	54.4	$5.6 \times 10^{-2}$	3.3
11	50000	108.8	$5.6 \times 10^{-2}$	5.5
12	39000	208	$5.6 \times 10^{-2}$	4.3
13	65000	400	$5.6 \times 10^{-2}$	7.1
14	8300	9.76	$4.1 \times 10^{-2}$	3.9

Table 2.1: Irradiation parameters for the different spots, Integrated (red) fluorescence intensity and electron dose and estimated NV<sup>-</sup> concentration for the different spots shown in Fig. 2.2.

a opposite signed flop (absent other effects angular momentum should be conserved). The  $T_1$  dependence on the external field is depicted in Fig. 2.4(a). An increase in relaxation rate can be observed at zero field. This can be explained by the fact that at zero field the energy matching condition is fulfilled for off-axis NV centers as well increasing the number of relaxation channels and thus decreasing the relaxation time  $T_1$ .

Fig. 2.4(b) shows the relaxation rate and  $\beta$  parameter dependence on the NV concentration. With increased NV concentration the relaxation rate increases and the distribution of relaxation rates (inferred from the  $\beta$  parameter). The increase in relaxation rate is near linear in concentration, which hints towards a dipole-dipole interaction dominated relaxation mechanism. The interaction strength scales as  $r^{-3}$ , where  $r$  is the distance between to NV centers. This distance however scales as  $[\text{NV}]^{-1/3}$  and the overall scaling is thus linear in concentration. This relaxation mechanism also explains the broadening in relaxation rates with increasing NV concentration. A simple model illustrates this well. Let us scatter 2000 and 3000 points randomly in a fixed volume. Fig. 2.5 shows a histogram of interaction strengths defined as  $1/r^3$ , where  $r$  is the distance between a defect and its nearest neighbor. One can easily see that both the average interaction strength and the width of the distribution increases with concentration.

A puzzling feature is how subdued the zero field resonance is, since there are 4 times as many relaxation partners than when the degeneracy is

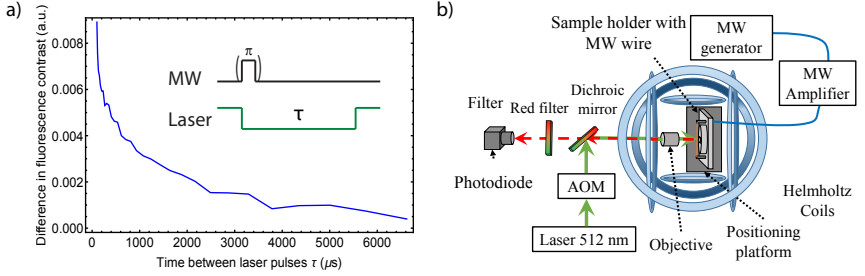


Figure 2.3: (a)  $T_1$  measurement pulse sequence and a typical fluorescence dependence on the free evolution time  $\tau$ . (b) Experimental setup to measure the relaxation time  $T_1$ .

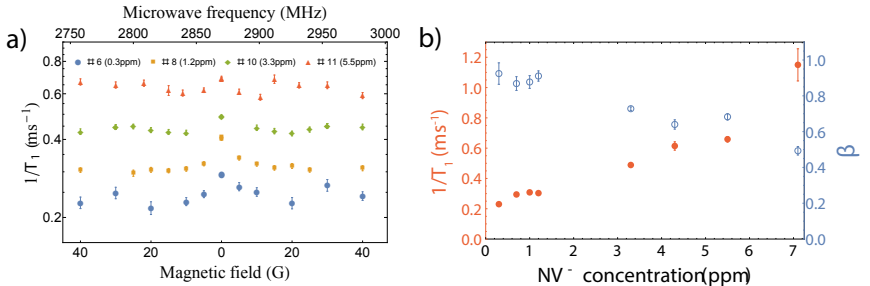


Figure 2.4: (a) Relaxation rate  $1/T_1$  as a function of NV concentration and applied magnetic field. (b) Effective relaxation rate and  $\beta$  parameter as a function of NV concentration.

lifted. Naively one would expect a proportional increase in relaxation rate (especially for the higher concentration spots where the dipolar relaxation contribution would be more significant). This can partly be explained by consider the fact that NV centers aligned along the same direction have a roughly  $1.5\times$  larger interaction energy than with those aligned along any of the other 3 axis, but this should still cause a  $3\times$  increase in the relaxation rate.

There are two effects that have not been accounted for in the experiment and that might influence the relaxation dynamics. First, is the NV charge state photodynamics. Under laser illumination the  $\text{NV}^-$  center has a probability of exciting the electron to the conduction band through a two-photon process where it can diffuse away and change the charge state of the defect to a  $\text{NV}^0$ . The reverse process where the  $\text{NV}^0$  center is converted back to  $\text{NV}^-$  is also possible. The equilibrium ratio of the

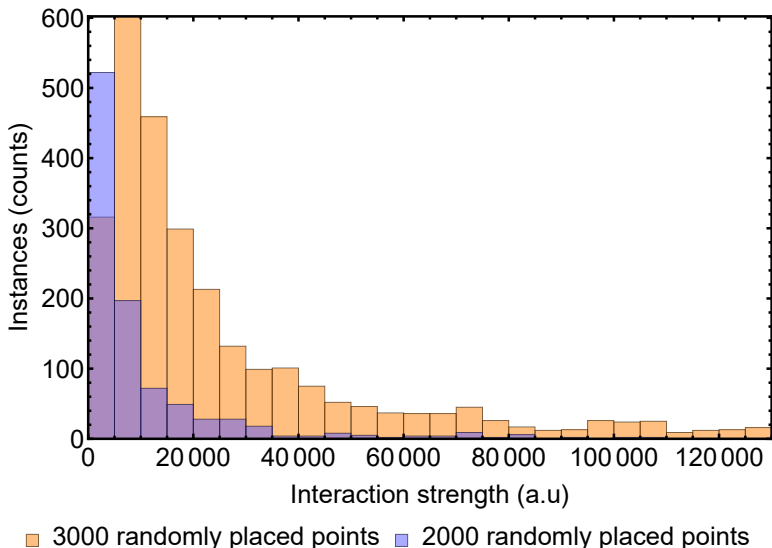


Figure 2.5: A histogram of interaction strength for 2000 and 3000 points randomly distributed in a fixed volume. The  $x$  axis shows the interaction strength and the  $y$  axis shows the frequency of points interacting with said strength with another defect.

two defects are dependent on the duty cycle of the applied laser illumination which changes by sweeping the free evolution time. To study this in more detail it would be necessary to monitor the spectra of the fluorescent radiation and compare the relative intensities of their respective zero phonon-lines.

The second effect that has not been accounted for is the formation of self-defects in diamond during electron irradiation. It is assumed that the vacancies formed during electron irradiation either form NV centers or are annealed out, however, it is possible that multi-vacancy defects are formed (two or more vacancies occupying adjacent lattice sites). Multi-vacancy defects are stable even at elevated temperatures and have low diffusion coefficients. These defects are also known to be paramagnetic possibly decreasing the NV relaxation times. To isolate this effect it would be useful to spatially correlate the  $T_1$  relaxation rates with birefringent activity indicative of lattice damage.

### 3 Magnetic microscopy with NV centers

A wide array of magnetic phenomena manifest itself only at the microscale. The research fields interested in understanding micro- and nano-magnetic behaviour range from geology [42], study of superconductive materials [43], spintronics [44] and medicine/biology [45]. Commonly used bulk magnetometry cannot capture these small scale effects. Existing micro-scale techniques each have their own drawbacks: magnetic force microscopy while having AFM spatial resolution is limited in terms of field of view (typically  $< 100 \mu\text{m}$ ) and poor sensitivity ( $> 10 \mu\text{T}$ ). SQUID based microscopes suffer from poor spatial resolution ( $\sim 150 \mu\text{m}$  [46]) when working with room-temperature samples. Magneto-optical Kerr effect (MOKE) microscopes need Faraday-active samples or deposition of such a layer on top of the sample which might perturb the system in hard to predict ways and is generally incompatible with biological systems.

The spatial resolution of a properly engineered ensemble diamond sensor is limited only by diffraction. This enables microscale magnetic resonance imaging at room temperature with a reported volumetric DC magnetic field sensitivity of  $34 \text{ nT}\mu\text{m}^{-3/2}\text{Hz}^{-1/2}$  with a theoretical sensitivity in the  $\sim 100 \text{ pT}\mu\text{m}^{-3/2}\text{Hz}^{-1/2}$  pT range [15] while keeping the cost of the setup under  $< 50\text{k USD}$ . To reach this kind of performance several technical challenges unique to the diamond platform must adequately addressed.

This chapter will discuss the basic working principles of a NV magnetic microscope, the best practices and technical challenges that need to be addressed to reach peak sensitivity, give an overview of recent groundbreaking work in the field, and discuss results from two specific imaging experiments studying chains of magnetic micro-particles and the magnetic properties of malarial hemozoin crystals.

Another intensively explored area of study in the field of NV quantum sensors are single NV scanning tip microscopy. This chapter will, however, omit any discussion on this subject focusing only on the microscopy detection modality.

## Basic components and principles of operation of the diamond magnetic microscope

The basic building blocks of the NV magnetic microscope are similar to the ODMR magnetometer discussed in section 1.2 and a typical setup (shown in Fig. 3.1) bears many resemblances to the one shown in Fig. 1.4. The procedure is also similar

- The magnetic sample is placed on top of the diamond. For micro- and nano-scopic samples even small stand-off values can introduce significant variations in the field strength at the NV-site so the deposition protocols should be designed with care to ensure precision and reproducibility.
- NV centers are excited and spin-polarized by green light either in an epifluorescence configuration as shown in Fig. 3.1 or from the side as shown in the the review by Levine and Turner et. al [46].
- An external field is applied along a particular NV axis (out of 4 possible directions) to simplify the spectra. Other configurations where the field is placed the (100) direction of the diamond or indeed in a random direction that does not lie in any of the symmetry planes of the crystal are also sometimes used. The former yields a higher sensitivity while working at low fields while the latter is useful in a vector-magnetometer implementation. In NV ensemble magnetometers some bias magnetic field is almost always applied as there is always some transverse strain coupling the  $|m_s = \pm 1\rangle$  resulting in a poor sensitivity near zero field.
- The applied microwave frequency is swept in synchronicity with the frame-rate of the camera. Usually this procedure is repeated many times to achieve the desirable per-pixel sensitivity. The result is a stack of fluorescence images at different applied microwave frequencies from which the spatial magnetic field distribution can be obtained.

There are however certain additional elements that are necessary to improve the performance of the microscope. In order to illuminate homogeneously a reasonable portion of the field-of-view usually a lens or a lens system is placed in the excitation beam path. The microwave field strength should also be uniform across the sample to avoid sensitivity losses due to power broadening (discussed in section 1.2). A commonly used and simple

approach is using a circular microwave trace deposited on a microscope cover-slip or the diamond itself. This ensures optical accessibility with reasonable power delivery while still maintaining a low AC quality factor - a pro rather than a con since power delivery uniformity across a broad frequency range is more important than power delivery efficiency.

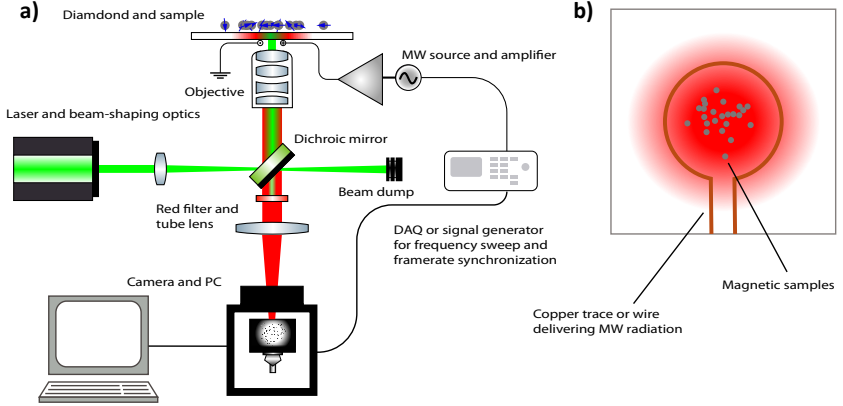


Figure 3.1: The magnetic resonance imaging setup. a) The schematic of an epifluorescence diamond microscope. The sample is usually placed on top off the diamond while the microscope is inverted. b) Top view of the diamond. The red area shows the illumination/fluorescence profile and the brown line is a deposited copper trace surrounding the field of view.

The magnetic field information extracted from the frequency-synchronized image stack can be understood by observing Fig. 3.2, which shows a simple model experiment where identical paramagnetic particles are placed on top of the diamond and the  $|m_s = 0\rangle \rightarrow |m_s = -1\rangle$  ground state spin transition is addressed (this determines the sign of the resonance frequency shift). As the frequency is swept closer to resonance the fluorescence intensity decreases. This happens faster for the paramagnetic particles as the field is slightly stronger in their vicinity and initially these regions appear dimmer. As the sweep continues these regions will eventually appear lighter than the background as the resonance has already been crested for the regions in the vicinity of the particles while the particle-free regions are lagging behind. After the sweep is complete the local magnetic field value can be obtained by performing per pixel fitting of the ODMR spectrum.

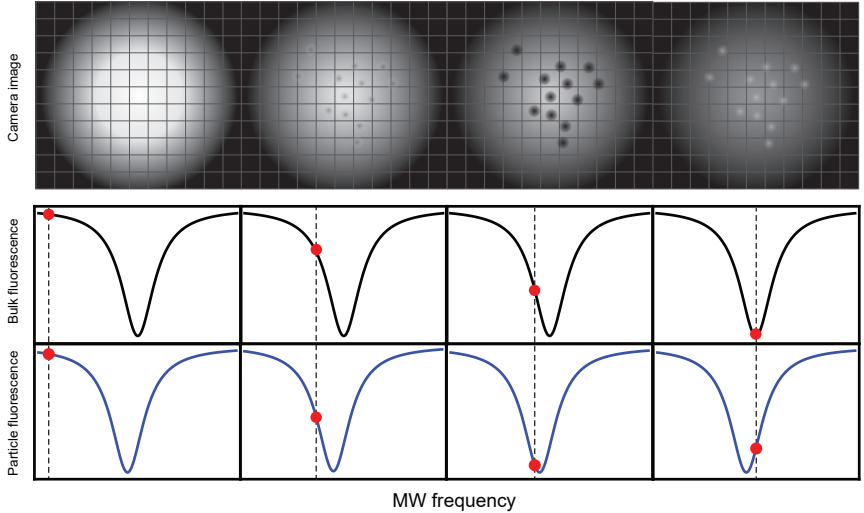


Figure 3.2: Magnetic image formation. Top row shows the image on the camera sensors corresponding to the detuning from resonance. Placed on top of the diamond are several paramagnetic particles. The bottom two rows show the fluorescence/MW frequency dependence for particle free regions (black) and regions in close vicinity to the particles (blue).

## Magnētisku daļiņu magnētiskā mikroskopija

The potency of the platform motivated the University of Latvia Laser Center in collaboration with the Laboratory of Magnetic Soft Materials to build a magnetic imaging microscope with the ultimate goal of studying the dynamics of magnetic microswimmers, more specifically, a microswimmer consisting of a chain of ferromagnetic and superparamagnetic particles connected by a strand of protein. Controllable micro-scale devices have the potential to significantly improve precision medicine through techniques such as targeted drug delivery and the magnetic variety addresses one of the key challenges in the field—sustained locomotion—by driving them via an external magnetic field that can penetrate tissue. However, the interactions between the different forces at play (fluid viscosity, elasticity of the swimmer, magnetic dynamics within the beads, etc.) are complicated and hard to decouple, a time-dependent magnetic field map could help shed light of the magnetic dynamics of microswimmers. The first step was obtaining the static magnetic field distribution of the particles forming

the swimmers. The diamond sensor was manufactured from a (100) face

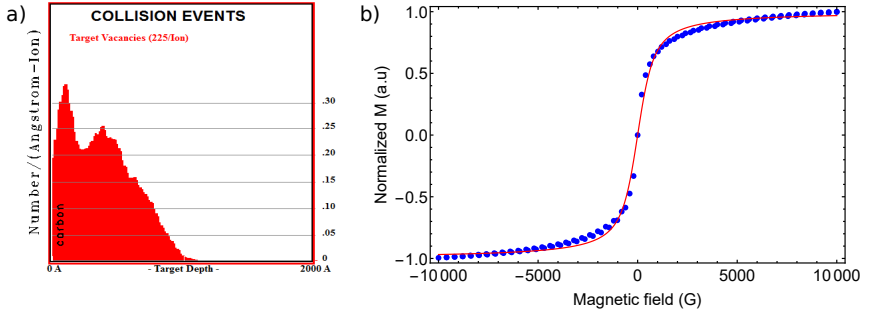


Figure 3.3: (a) Simulētais vakanču-dziļuma sadalījums veicot  $^{14}\text{N}^+$  jonu implantāciju dimantā ar kinētiskajām enerģijām: 10 keV, 35 keV un 60 keV. (b) Histerēzes likne superparamagnētiskām daļiņu tilpuma paraugam, kas uzņemta ar vibrējošā parauga magnetometru. Sarkanā līnija ir piedzītā Lanžēvena funkcija, no kuras iespējams noteikt vidējo daļiņu magnētisko momentu.

CVD type IIa diamond with a negligible nitrogen content. The chip was implanted with  $^{14}\text{N}^+$  ions with 3 different energies—10 keV, 35 keV and 60 keV—creating a vacancy/nitrogen depth distribution shown in Fig. 3.3(a) with a mean thickness of around 500 nm. Subsequent annealing at  $800^\circ\text{C}$  should not have caused any further broadening of the final NV depth distribution as the diffusion activation energy of substitutional nitrogen is large. Three types of magnetic particles were used: 4- and 2-  $\mu\text{m}$  diameter  $\text{CrO}_2$  ferromagnetic core-shell particles and 500-nm-diameter  $\text{Fe}_2\text{O}_3$  superparamagnetic particles. The latter consist of a polystyrene shell that encases an emulsified ensemble of  $\text{Fe}_2\text{O}_3$  particles with a mean diameter of  $\sim 10\text{nm}$ . This means that the particles can still remain superparamagnetic rather than ferromagnetic yet have a higher magnetic moment. The ensemble properties were characterized by vibrating sample magnetometry (VSM) shown in Fig. 3.3(b). The magnetic moments of the paramagnetic particles were extracted directly from the magnetization curve by fitting it with a Langevine function  $L$ :

$$L(\alpha) = \coth(\alpha) - \frac{1}{\alpha} \quad (3.1)$$

$$\alpha = \frac{mH}{k_B T},$$

where  $m$  is the magnetic moment,  $H$ , magnetic field,  $k_B$ , Boltzmann constant, and  $T$ , the temperature.

The experimental setup and procedure is the same as described in the previous section with one key difference. The applied biasing magnetic field was directed not along a particular axis but along the [100] direction, where the magnitude of the field projection on the NV axis is identical for all 4 spatial directions. When working at small magnetic fields this yields a better sensitivity due to the nearly four-fold increase in signal contrast.

The obtained results are shown in Fig. 3.4. As can be seen the correlation between optical images and magnetic is very strong. Each particle produces a magnetic field and particles show a spatial field distribution characteristic of a dipole. It is also possible to estimate the magnetic momenta of individual particles from these images. If we assume the particles are ideal dipoles the magnetic field they produce can be written as:

$$\mathbf{B} = \frac{\mu_0}{4\pi} \left( \frac{3\mathbf{r}(\mathbf{m} \cdot \mathbf{r})}{r^5} - \frac{\mathbf{m}}{r^3} \right), \quad (3.2)$$

where  $\mathbf{m}$  is the magnetic moment, and  $\mathbf{r}$  is a vector connecting the NV center to the location of the magnetic dipole. The observed magnetic field distribution is broadened due to the finite resolution of the microscope. The original distribution is recoverable by deconvolving the magnetic image. This is possible because the point-spread function can be faithfully approximated with a Gaussian function with a full-width at half maximum is 313 nm and which can be assumed to be constant across the whole field of view. The Richardson-Lucy algorithm was used to perform the deconvolution. Afterwards a nonlinear fit was performed to obtain the magnetic moments with the following fit function:

$$\mathbf{e}_{[100]} \cdot \mathbf{B} = \frac{\mu_0}{4\pi} \left( \frac{3\mathbf{e}_{[100]} \cdot \mathbf{r}(\mathbf{m} \cdot \mathbf{r})}{r^5} - \frac{\mathbf{e}_{[100]} \cdot \mathbf{m}}{r^3} \right). \quad (3.3)$$

$\mathbf{e}_{[100]}$  is a unit vector coincident with the direction of the applied bias magnetic field and the surface normal of the diamond chip. The obtained fit parameters are summarized in table 3.1. The obtained fit parameters

Particle type	ferromagnetic	ferromagnetic	superparamagnetic
diameter $d$ ( $\mu\text{m}$ )	4 $\mu\text{m}$	2 $\mu\text{m}$	500 nm
Expected $ \mathbf{m} $ ( $\text{Am}^2$ )	$2.3 \times 10^{-13}$	$2.6 \times 10^{-14}$	$1.6 \times 10^{-15}$
Fitted $z-d/2$ ( $\mu\text{m}$ )	$1.4 \pm 0.1$	$1.3 \pm 0.1$	$3.6 \pm 0.1$
Fitted $ \mathbf{m} $ ( $\text{Am}^2$ )	$(6.0 \pm 0.1) \times 10^{-14}$	$(7.9 \pm 0.2) \times 10^{-15}$	$(1.2 \pm 0.1) \times 10^{-14}$

Table 3.1: Magnetically relevant fit parameters for the different magnetic particles investigated in this work.

exhibit several surprising features. First of all, the value of  $z - d/2$  which characterizes the sensor-source distance is significantly larger (especially

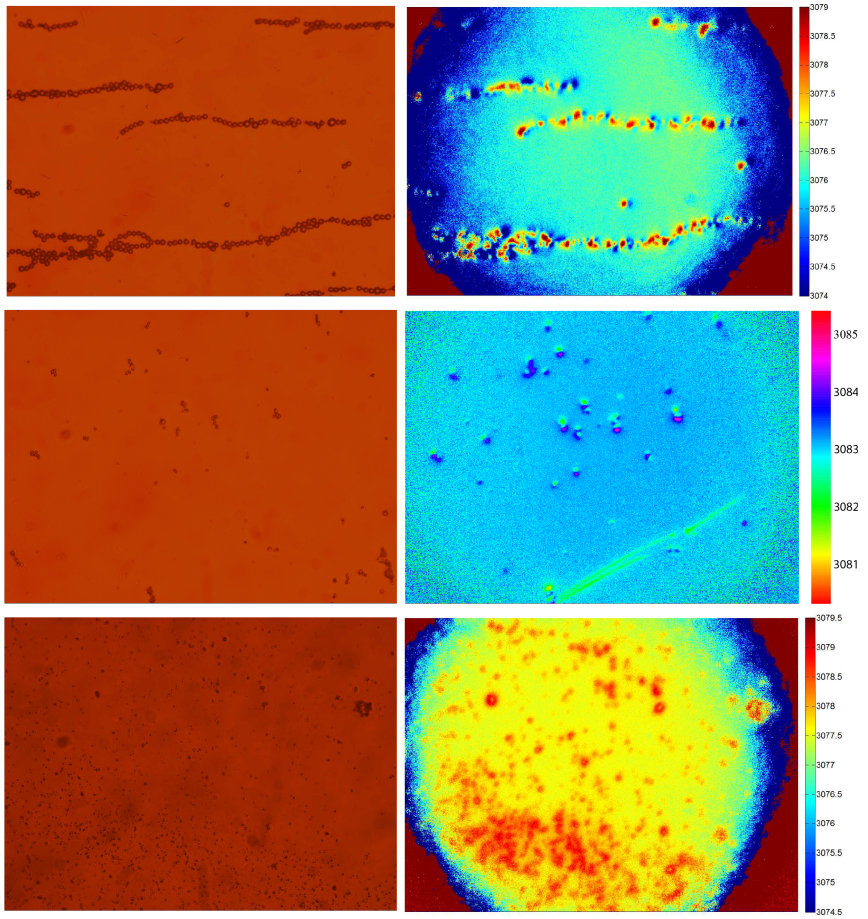


Figure 3.4: optical and magnetic images of 4  $\mu\text{m}$ , 2  $\mu\text{m}$  ferromagnetic and 500 nm superparamagnetic particles. The magnetic field measured in frequency units  $f = \gamma B$ , where  $\gamma = 2.803 \text{ MHz/G}$ .

for the superparamagnetic particle) than the expected value of  $\sim 0$  nm where the particle is resting directly on the surface of the diamond. This stand-off distance is not just a mistake due to the numerical procedures employed as the observed magnetic features are also broader than suggested by a simple forward model according to expression 3.2. A possible culprit could be residual solute from the sodium azide and phosphate pH buffer solution in which the particles were suspended. Based on the solute concentration given by the vendor (correcting for a 50x dilution with water—a part of the preparation process), the deposited volume of  $10\mu\text{L}$  would create a  $1.2\ \mu\text{m}$  thick layer of solid residue across the diamond which is close to the fit values obtained for the ferromagnetic particles. For the 500 nm superparamagnetic particles the discrepancy is even more pronounced however exact solution composition for the superparamagnetic particles is unknown precluding a similar analysis.

The magnetic moment values obtained from the fit also significantly deviate from the ensemble measurements both over- and under-shooting the expected values from ensemble measurements 4-10 times. While some variation in the magnetic moment values is expected the results obtained lie well outside the specification given by the manufacturer. These discrepancies indicative of uncontrolled-for systematics in the experimental setup.

This was the first setup of its type in Latvia and the as a result of this research several key areas of improvement in the experimental design were identified:

- It is important to take into account the decrease in optical power density when illuminating a large field of view. Insufficient pumping power leads to poor NV spin polarization and low ODMR contrast.
- Microwave and framerate synchronization should be done in hardware rather than in software. The software implementation lead to poor acquisition duty cycle and poor sensitivity in real terms. Modern scientific cameras offer a wide variety of configurable event triggers that can be used to significantly improve the measurement up-time.
- Originally the microwave power was switched on and off in an alternating fashion to enable normalization of the fluorescence image against the case where no microwaves were applied. This was done to suppress effects from a spatial inhomogeneity of the illuminating laser. This procedure however had the adverse effects of causing mechanical vibrations in the sample and are a probable culprit for the obtained broader-than-expected magnetic field distributions.

## Magnetic imaging of malarial hemozoin

The power of optimized experimental procedures was demonstrated in a later work probing the properties of hemozoin [47]. Hemozoin is an organic crystal formed by blood-feeding parasites. Amongst such parasites is *Plasmodium* that causes malaria. A product of the parasites digestion of haemoglobin is heme, a substance toxic to cells and to the parasite itself. The parasite accretes free heme into insoluble hemozoin crystals to avoid poisoning itself. Anti-malarial drugs disrupt the the formation of hemozoin and cause the parasites to kill themselves. The NV diamond microscope could theoretically probe the hemozoin formation/disruption dynamics in living *Plasmodium*-infected cells. However, the first step is to produce magnetic images of individual hemozoin crystals. The author's contribution to this work was limited to implementing the control and automation software and discussing the results.

In this experiment a type Ib diamond with a  $[N] \approx 50$  ppm was used. It was electron irradiated and annealed forming around a 200 nm thick NV layer near the diamonds surface. A 532 nm diode pump solid state laser produced 200 mW of optical power at the exit of the objective. It was focused to a spot 40  $\mu\text{m}$  in diameter. The power density was thus around  $500\times$  larger than in the experiment described in the previous section. Microwave sweep-camera synchronization was realized in hardware, where the camera sent periodic trigger pulses to a data acquisition card which in turn generated a ramp voltage passed to the frequency modulation port of the microwave generator.

The device demonstrated a per-pixel sensitivity of  $8.4 \mu\text{T Hz}^{-1/2}$ , an order of magnitude improvement with the previous design. The obtained magnetic susceptibility estimates for the hemozoin crystals agreed with those reported in literature studying ensembles [48, 49].

The obtained results are shown in Fig. 3.5. These results demonstrate the benefits of knowing the information on all the members of an ensemble. Almost all the hemozoin crystals behave as paramagnets, showing a linear response as a function of the applied field, however some of the show superparamagnetic behavior - an effect easily missed in an ensemble measurement.

The improvements in measurement quality and sensitivity in the second iteration of the device provides an impetus to revisit efforts of studying the magnetic dynamics of micro-swimmers.

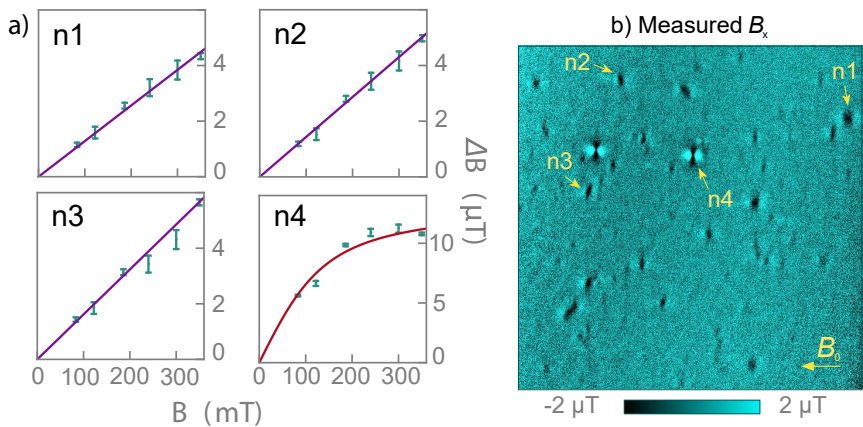


Figure 3.5: (a) Magnetic fields produced by individual particles (marked in figure (b)) as a function of external field. Particle n4 shows both saturation and generates a higher field - both properties indicative of superparamagnetism. (b) Magnetic image of hemozoin crystals deposited on the diamonds surface at a bias field of  $B_0 = 350 \text{ mT}$ .

## 4 Nuclear magnetic resonance spectroscopy with NV centers

Measuring magnetic fields of submicron volumes might seem like an impressive achievement but only begins to utilize the possibilities opened up by NV centers. The ease with which NV centers can be coherently manipulated with microwaves, means that the AC sensitivity can be pushed to the nano- and picotesla level. This opens up the possibility of chemical analysis of picoliter volumes using the techniques of nuclear magnetic resonance (NMR).

While the information on the molecular composition and structure obtainable from NMR spectra is very rich in detail, the technique imposes strict demands on sensor performance. Both in terms of sensitivity when detecting the nano- to pico-tesla signals and in terms of spectral resolution which is in the parts-per-million to parts-per-billion range.

Most modern NMR spectrometers use sensitive induction coils to detect the oscillating magnetic fields. Many research groups have worked on coil geometries, accompanying electronics and experimental design optimization with the goal of shrinking the sensor volume and the necessary amount of analyte. There are however fundamental restrictions related to susceptibility mismatches and resonator quality factors that motivate the search for alternative detection modalities.

The NV centers have already demonstrated magnetic detection with optical resolution. Improvements in sensitivity from advanced measurement protocols and diamond fabrication optimization could potentially enable chemical investigation with optical resolution.

This section will give a brief introduction to the basic physical concepts underlying NMR spectroscopy and summarize two NV NMR experiments probing statistical and thermal nuclear spin polarization.

## NMR spectroscopy

In NMR spectroscopy the magnetic signals are produced by the magnetic moments of the nuclei. If a nucleus has non-zero spin, it possesses a magnetic un angular momentum. If the spin is polarized transverse to and external field it will start to precess around said field at the Larmor frequency  $\omega_0 = \gamma B$ , where  $\gamma$  is the gyromagnetic ratio. Each nucleus has a unique gyromagnetic ratio which means that magnetic signals produced by, for example  $^{13}\text{C}$  nuclei will appear at a different spectral band than those produced by  $^1\text{H}$  nuclei.

This fact by itself does not explain how chemical information can be inferred from NMR spectra, indeed, there are simpler ways to ascertain the elemental composition of an analyte. The chemical information is hidden at an energy scale much smaller than the Zeeman splitting, the interactions of interest are chemical shift and J-coupling and are due to the nuclei interacting with the surrounding electrons. Chemical shift arises due to a small additional magnetic field component generated by electrons moving in the applied bias field. This additional field is proportional to the applied bias field and is usually given in relative units such as ppm. J-coupling is a constant shift (independent of applied bias field) and arises by nuclear-nuclear interactions mediated by the electrons in the bond (a more detailed description is presented in the dissertation).

Fig. 4.1 shows the  $^1\text{H}$  NMR spectrum of ethanol. Three distinct color-coded subgroups of peaks are visible. This separation arises due to the different chemical shifts experienced by different nuclei. The finer splitting within each subgroup is due to J coupling. As can be seen even for a simple molecule the NMR spectra is somewhat complicated. Interpretation of spectra made easier by two facts, first, the J-couplings are usually spatially localized and diminish rapidly as the number of bonds between interacting nuclei increase, second, the chemical shifts of most functional groups are well known and vary little between compounds.

## Statistiskās polarizācijas spektroskopija ar NV centriem

The first papers reporting on ensemble NV NMR signals from spins not belonging to the diamond host [50, 51] exploited the effect that if the effective sensing NMR is very small the stochastic polarization (i.e. the probability that at any point in time there might be more spins pointing

## Ethanol

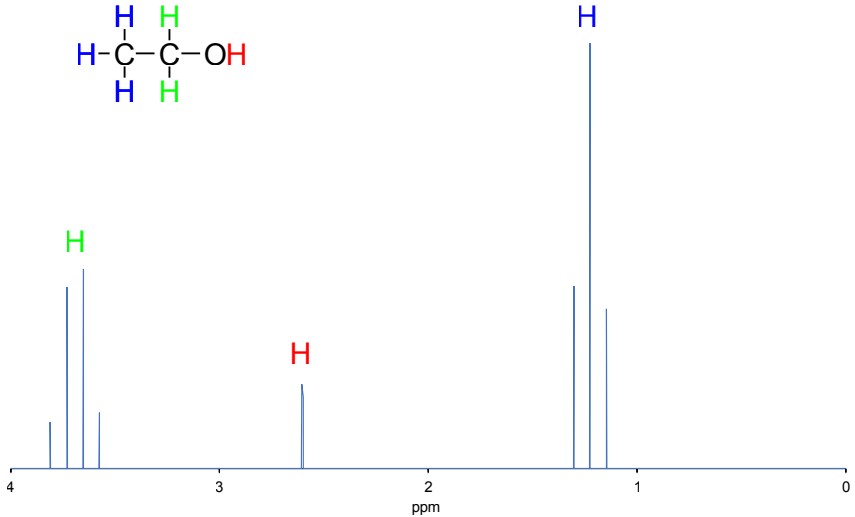


Figure 4.1: The  $^1\text{H}$  spectrum of ethanol.

along the  $+x$  direction than the  $-x$  direction) can become substantial. A comparison between statistical polarization and thermal polarization (the small net polarization due to the energy difference between the Zeeman sublevels) for protons in water at two different field strengths is shown in Fig. 4.2. As can be seen as the volume shrinks below  $1\ \mu\text{m}^3$  the field from the statistically polarized protons rapidly increases.

The effective sensing volume of an NV center is determined by the sensor-analyte distance. Fig. 4.3 shows a side-by-side view of two NV centers at different depths. Each spin a magnetic dipole generating a field that falls off as  $1/r^3 \sim 1/V$ , where  $V$  is the sensing volume, the number of statistically polarized spins scales as  $\sqrt{V}$  so the overall scaling of the signal strength due to statistical polarization versus sensing volume is  $V^{-1/2}$ . For thermal polarization this quantity is constant as the number of polarized spins is linear in volume and the overall signal strength is constant.

As the average NV depth must be very small this constrains the average depth of the NV ensemble. This means that the amount of fluorescence is also weak leading to a poorer shot-noise limited performance. The results of this section come from a paper[7] trying address this challenge by nanostructuring the diamond surface in increase the NV density per unit are while still maintaining the NV-surface distance small. This was done by fabricated grating like structures (Fig. 4.4(a)) on the diamond

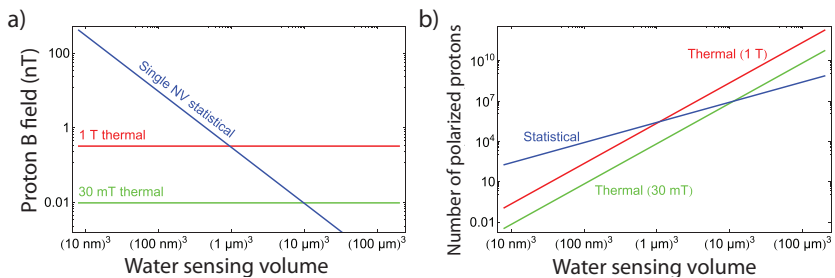


Figure 4.2: Thermal vs statistical polarization; a) the magnetic field produced by the target spins as a function of volume b) the number of polarized spins as a function of volume.

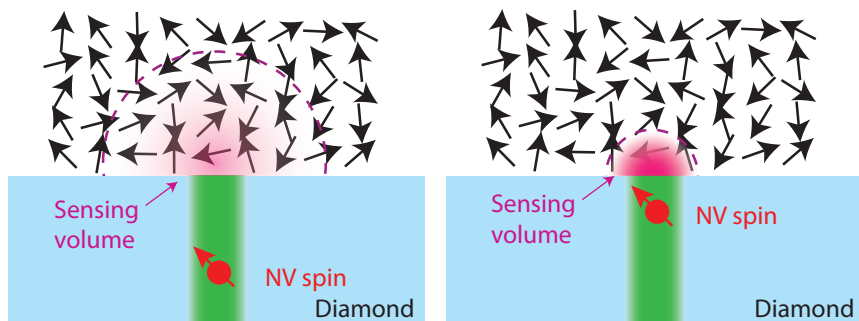


Figure 4.3: Effective sensing volume for NV centers at two different depths. For shallow NVs the majority of the signal is contributed by a few strongly interacting spins near the diamond surface.

surface. Fig. 4.4(b) shows the fluorescence intensity comparison between a nanostructured and flat diamonds and Fig. 4.4(c) depicts a confocal image of dye-stained water on top of the diamond showing good wetting and penetration within the grooves.

An XY8-N correlation sequence was used to detect the AC magnetic field (more details in the dissertation). The time-dependent signal from Fomblin oil (a viscous oil with high fluorine content) can be seen in Fig. 4.5(a) and its Fourier transform is shown in Fig. 4.5(b). The minimum detectable spin concentration in one second (defined as the spin concentration leading to a signal-to-noise ratio of 3:1) is  $\rho_{\min} = 40 \pm 2 \times 10^{24}$  spins/liter which is equivalent to 4 picomoles for our addressed volume. Unfortunately there is a fundamental issue plaguing statistical NV NMR. It is illustrated in Fig. 4.5(c). To detect the frequency of the precessing spin with a high spectral accuracy, the interrogation time must be long

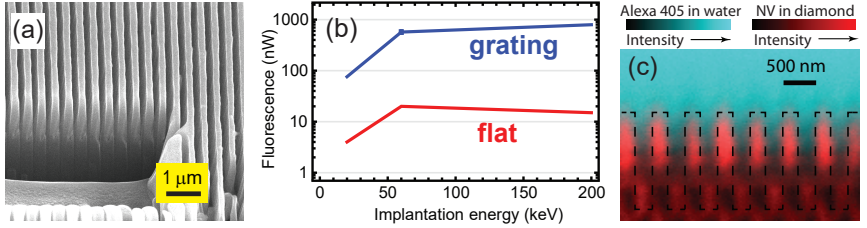


Figure 4.4: Nanostructured diamond surface for higher SNR. a) SEM image of the etched grooves. b) Performance enhancement of nanostructured vs flat diamond. The fluorescence level is significantly higher due to the larger number of NV centers in contact with the analyte in the same field of view. c) Confocal image of the diamond with dye-stained water dispersed on top of it. The dashed lines represent the diamond-water boundary.

enough ( $\Delta t \Delta \omega \geq 1/2$ ). The interrogation time is limited by the time it takes for a nucleus to diffuse away from the NV detection volume. The measurement time  $\tau$  can be expressed as:

$$\tau = \frac{2d_{NV}^2}{D}, \quad (4.1)$$

where  $d_{NV}$  is the depth of the NV center and  $D$  is the diffusion coefficient of the analyte. This time can be extended by increasing the viscosity of the fluid, but this eventually leads to broadening due to anisotropic dipole-dipole couplings, which do not average away effectively if the molecule tumbling rate is slow. The linewidths obtained for glycerol on this setup are of kHz order. By working at very high fields (compared to most published NV research) and using viscous samples Aslam et al. [52] did achieve chemical resolution NV NMR spectroscopy but the technical complexity of the experiment mostly outweighs any gains from the higher statistical polarization.

## Microscale sensing of thermal polarization

While promising on account of their larger SNRs, achieving a high spectral resolution with this technique is an enormous technical challenge. As a result, we decided to pivot to NMR based on thermally polarized spin signals. These signals are much weaker, but do not suffer from the diffusion issue as all the spins are in phase. The field magnitude generated by an

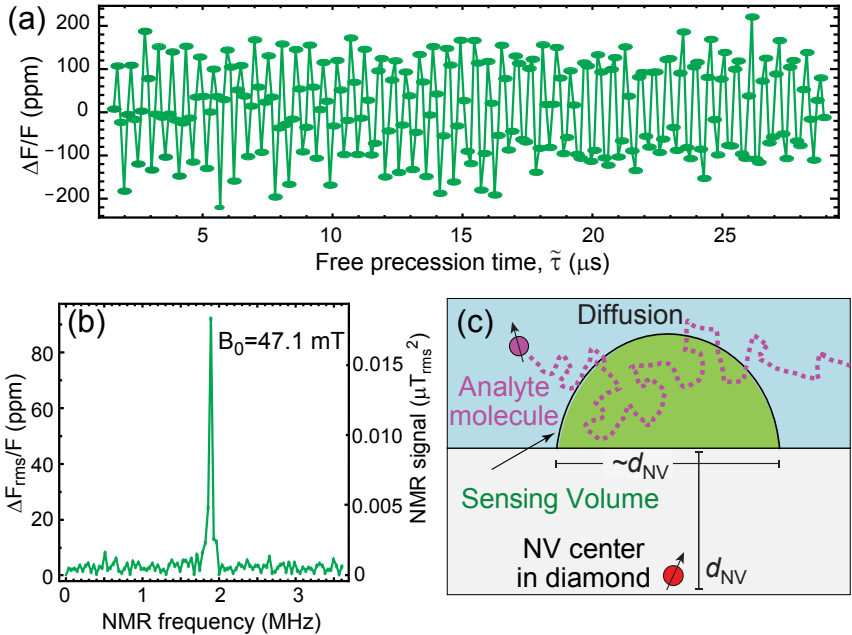


Figure 4.5: (a) Time-domain NV NMR signal for Fomblin oil. (b) Fourier transform of the signal shown in (a). (c) Nuclear spin diffusion away from the NV center. This limits the correlation time between the NV center and the nucleus fundamentally limiting the attainable spectral resolution.

ensemble of thermally polarized spins can be estimated as:

$$B_{\text{therm}} \sim \frac{\mu_0}{4\pi} \frac{h^2 \gamma^2 B_0 \rho}{4k_B T}. \quad (4.2)$$

The decoupling sequences for AC sensing described in the previous section are hard to implement if the nuclear Larmor frequencies are larger than a 100-200 MHz as the requirements on both pulse duration and power delivery become very stringent. For proton spins the equivalent field is around 2000 G. By plugging the variable into equation 4.2 the field generated by protons in pure water at this field is around 600 pT. To increase the signal strength the NV sensors was integrated into a microfluidic system with the goal of separating the polarization and sensing phases of the experiment. A 1.5 T permanent magnet Hallbach array was used for polarization while the detection of the signal was realized at 13 mT (generated by a pair Helmholtz coils) where both the diamond sensor performance and field homogeneity are much more easily optimized. The prepolarization principle is depicted in Fig. 4.6. The analyte is first moved into the Hallbach array where it is allowed to reach thermal equilibrium, then it is quickly shuttled to the center of the Helmholtz coils. Quickly in this case means in a time that is smaller than the  $T_1$  time of the analyte.

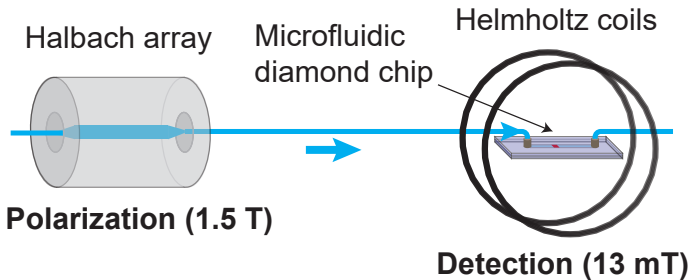


Figure 4.6: The prepolarization setup. Analyte is flown through a high-magnetic field area generated by a Hallbach array. The analyte polarizes in this region and is then quickly shuttled (with a shuttling time lower than the  $T_1$  of the analyte) to the sensing area.

The sensor parameters were calibrated on a water proton signal. The obtained concentration sensitivity is  $\rho_{\text{min}} \approx 1.6 \times 10^{25}$  and the obtained spectral resolution is  $\Delta\nu = 0.65 \text{ Hz}$  multiple orders of magnitude above the diffusion limit of the statistical technique. We believe that the resolution bottleneck is the temporal stability of the current supply driving the Helmholtz coils.

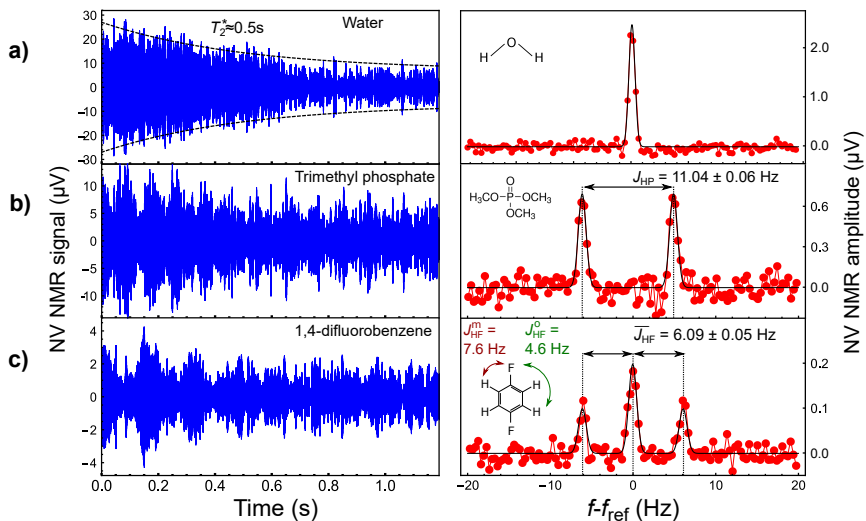


Figure 4.7: Time domain (left column) and frequency domain (right column) NV NMR signals of (a) water, (b) trimethylphosphate (TMP), and (c) 1,4-difluorobenzene (DFB). The signals are averages of  $\sim 1000$  traces equivalent to a total acquisition time of  $\sim 1$  h. Each of the peaks are fit with Gaussian functions to obtain the resonance frequencies. When fitting the TMP data the peak amplitudes are constrained to be equal while for DFB a 1:2:1 amplitude ratio is enforced.

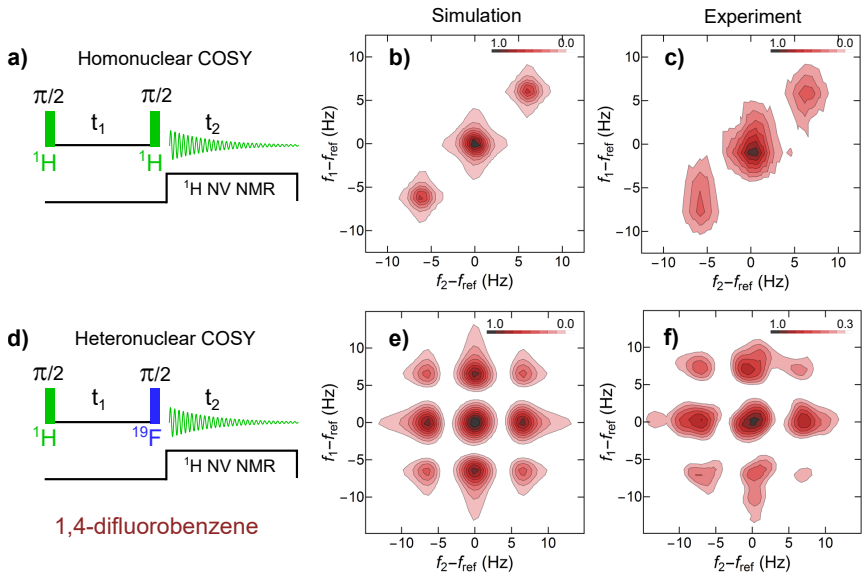


Figure 4.8: (A) Homonuclear COSY pulse sequence. (B) simulated spectrum. (C) Experimental NV NMR spectrum. (D) Modified heteronuclear COSY sequence which shows off-diagonal peaks in both the simulation (E) and experiment (F).

The high sensitivity and spectral resolution enabled us to perform two-dimensional NV NMR spectroscopy on an external analyte for the first time. There exists a broad range of multi-dimensional NMR techniques but for this experiment we chose one of the technically least taxing - a correlation spectroscopy (COSY) experiment on 1,4-difluorobenzene. Two different pulse sequences were realized the spectra of which were first simulated by unitary evolution of the density matrix and introducing relaxation by multiplying the oscillating spin projection expectation value with a decaying exponential. Modeling was performed in the Matlab package SPINACH [53]. The pulse sequences, modeled spectra and experimental results are summarized in Fig. 4.8.

## 5 Conclusions

The NV center in diamond has exceptional sensing capabilities and research in the field has been actively pursued by a large number of research groups worldwide. New detection modalities and performance improvements in terms of scale, sensitivity, and resolution sometimes spanning orders-of-magnitude are being published with a high frequency indicative of the potential of the platform. Additionally the fields in which the NV sensor is already being used as a sensor has also expanded considerably in the last few years ranging from biology, to geology, to electronics and material science. There are a large amount of tunable parameters and a wide array of experiment design approaches that affect the sensor performance and must be tailored to the particular problem under investigation. This work explored both parameter and design spaces of NV sensors.

In the first part of this work the dependence of the relaxation dynamics on the NV center concentration was studied. The concentration dependence of both the relaxation rate and rate distribution strongly hinted at a dipole-dipole interaction based relaxation model. However there were several features that still remain unexplained. First the amplitude of the zero field resonance compared to the relaxation rate at non-zero field was too small to be entirely explained by NV-NV dipole-Dipole relaxation. A hypothesis was put forward suggesting that self-defects formed during the electron irradiation could also play a role in the NV  $T_1$  relaxation. In a future experiment it would be useful to spatially correlate relaxation rates with regions of higher birefringent activity indicative of more lattice damage.

Chapter of the dissertation discussed the NV magnetic microscope that was employed to study the magnetic properties of ferro- and paramagnetic beads with the hope of eventually studying time-dependent magnetic signals. The obtained magnetic images showed good optical-magnetic correlation but poor quantitative performance making us question whether there might be some sources of systematic errors in the experiment. Several key areas of improvement in the experimental design were identified and it was shown that by implementing these steps a per-pixel sensitivity of

$8.4\mu\text{T}/\text{Hz}^{-1/2}$  could be achieved. These results are very promising and the obtained sensitivity could enable time-resolved magnetic measurements of micro-swimmers from ferromagnetic beads.

In the final chapter of this work the NV NMR spectrometer was discussed. The magnetic sensitivity and spectral resolution realized was good enough to enable the detection and publishing of the first-ever 2D NV NMR spectra on an external analyte.

## Bibliography

- <sup>1</sup>A. Acín, I. Bloch, H. Buhrman, T. Calarco, C. Eichler, J. Eisert, D. Esteve, N. Gisin, S. J. Glaser, F. Jelezko, S. Kuhr, M. Lewenstein, M. F. Riedel, P. O. Schmidt, R. Thew, A. Wallraff, I. Walmsley, and F. K. Wilhelm, “The quantum technologies roadmap: a european community view”, *New Journal of Physics* **20**, 080201 (2018).
- <sup>2</sup>“Quantum leaps - subatomic opportunities”, *The Economist* (2017).
- <sup>3</sup>C. L. Degen, F. Reinhard, and P. Cappellaro, “Quantum sensing”, *Reviews of Modern Physics* **89**, 035002 (2017).
- <sup>4</sup>R. LaRose, “Overview and comparison of gate level quantum software platforms”, arXiv:1807.02500 [quant-ph] (2018).
- <sup>5</sup>G. Balasubramanian, P. Neumann, D. Twitchen, M. Markham, R. Kolesov, N. Mizuochi, J. Isoya, J. Achard, J. Beck, J. Tissler, V. Jacques, P. R. Hemmer, F. Jelezko, and J. Wrachtrup, “Ultralong spin coherence time in isotopically engineered diamond”, *Nature Materials* **8**, 383–387 (2009).
- <sup>6</sup>N. Bar-Gill, L. M. Pham, A. Jarmola, D. Budker, and R. L. Walsworth, “Solid-state electronic spin coherence time approaching one second”, *Nature Communications* **4**, 1743 (2013).
- <sup>7</sup>P. Kehayias, A. Jarmola, N. Mosavian, I. Fescenko, F. M. Benito, A. Laraoui, J. Smits, L. Bougas, D. Budker, A. Neumann, S. R. J. Brueck, and V. M. Acosta, “Solution nuclear magnetic resonance spectroscopy on a nanostructured diamond chip”, *Nature Communications* **8**, 188 (2017).
- <sup>8</sup>D. J. McCloskey, N. Dontschuk, D. A. Broadway, A. Nadarajah, A. Stacey, J.-P. Tetienne, L. C. L. Hollenberg, S. Prawer, and D. A. Simpson, “Enhanced widefield quantum sensing with nitrogen-vacancy ensembles using diamond nanopillar arrays”, arXiv:1902.02464 [cond-mat, physics:physics] (2019).
- <sup>9</sup>T. R. Anthony and W. F. Banholzer, “Properties of diamond with varying isotopic composition”, *Diamond and Related Materials, Proceedings of the Second European Conference on Diamond, Diamond-like and Related Coatings* **1**, 717–726 (1992).

- <sup>10</sup>A. Jarmola, Z. Bodrog, P. Kehayias, M. Markham, J. Hall, D. J. Twitchen, V. M. Acosta, A. Gali, and D. Budker, “Optically detected magnetic resonances of nitrogen-vacancy ensembles in  $^{13}\text{C}$ -enriched diamond”, *Physical Review B* **94**, 094108 (2016).
- <sup>11</sup>E. Bauch, S. Singh, J. Lee, C. A. Hart, J. M. Schloss, M. J. Turner, J. F. Barry, L. Pham, N. Bar-Gill, S. F. Yelin, and R. L. Walsworth, “Decoherence of dipolar spin ensembles in diamond”, arXiv:1904.08763 [physics, physics:quant-ph] (2019).
- <sup>12</sup>D. Farfurnik, N. Alfasi, S. Masis, Y. Kauffmann, E. Farchi, Y. Romach, Y. Hovav, E. Buks, and N. Bar-Gill, “Enhanced concentrations of nitrogen-vacancy centers in diamond through TEM irradiation”, *Applied Physics Letters* **111**, 123101 (2017).
- <sup>13</sup>Y.-C. Chen, P. S. Salter, S. Knauer, L. Weng, A. C. Frangeskou, C. J. Stephen, S. N. Ishmael, P. R. Dolan, S. Johnson, B. L. Green, G. W. Morley, M. E. Newton, J. G. Rarity, M. J. Booth, and J. M. Smith, “Laser writing of coherent colour centres in diamond”, *Nature Photonics* **11**, 77 (2016).
- <sup>14</sup>C. Santori, P. E. Barclay, K.-M. C. Fu, and R. G. Beausoleil, “Vertical distribution of nitrogen-vacancy centers in diamond formed by ion implantation and annealing”, *Physical Review B* **79**, 125313 (2009).
- <sup>15</sup>J. F. Barry, M. J. Turner, J. M. Schloss, D. R. Glenn, Y. Song, M. D. Lukin, H. Park, and R. L. Walsworth, “Optical magnetic detection of single-neuron action potentials using quantum defects in diamond”, *Proceedings of the National Academy of Sciences* **113**, 14133–14138 (2016).
- <sup>16</sup>P. Balasubramanian, C. Osterkamp, Y. Chen, X. Chen, T. Teraji, E. Wu, B. Naydenov, and F. Jelezko, “Dc magnetometry with engineered nitrogen-vacancy spin ensembles in diamond”, *Nano Letters* (2019).
- <sup>17</sup>M. V. Hauf, P. Simon, N. Aslam, M. Pfender, P. Neumann, S. Pezzagna, J. Meijer, J. Wrachtrup, M. Stutzmann, F. Reinhard, and J. A. Garrido, “Addressing single nitrogen-vacancy centers in diamond with transparent in-plane gate structures”, *Nano Letters* **14**, 2359–2364 (2014).
- <sup>18</sup>B. Grotz, M. V. Hauf, M. Dankerl, B. Naydenov, S. Pezzagna, J. Meijer, F. Jelezko, J. Wrachtrup, M. Stutzmann, F. Reinhard, and J. A. Garrido, “Charge state manipulation of qubits in diamond”, *Nature Communications* **3**, 729 (2012).
- <sup>19</sup>Y. Mita, “Change of absorption spectra in type-*IIb* diamond with heavy neutron irradiation”, *Physical Review B* **53**, 11360–11364 (1996).

- <sup>20</sup>M. W. Doherty, N. B. Manson, P. Delaney, F. Jelezko, J. Wrachtrup, and L. C. L. Hollenberg, “The nitrogen-vacancy colour centre in diamond”, *Physics Reports*, The nitrogen-vacancy colour centre in diamond **528**, 1–45 (2013).
- <sup>21</sup>J. H. N. Loubser and J. A. v. Wyk, “Electron spin resonance in the study of diamond”, *Reports on Progress in Physics* **41**, 1201–1248 (1978).
- <sup>22</sup>J. Loubser and J. Van Wyk, “Optical spin-polarisation in a triplet state in irradiated and annealed type 1b diamonds”, *Diamond Research*, 11–14 (1977).
- <sup>23</sup>L. M. Pham, “Magnetic field sensing with nitrogen-vacancy color centers in diamond”, PhD thesis (Harvard University, May 1, 2013).
- <sup>24</sup>R. Hanson, O. Gywat, and D. D. Awschalom, “Room-temperature manipulation and decoherence of a single spin in diamond”, *Physical Review B* **74**, 161203 (2006).
- <sup>25</sup>A. M. Edmonds, U. F. S. D’Haenens-Johansson, R. J. Cruddace, M. E. Newton, K.-M. C. Fu, C. Santori, R. G. Beausoleil, D. J. Twitchen, and M. L. Markham, “Production of oriented nitrogen-vacancy color centers in synthetic diamond”, *Physical Review B* **86**, 035201 (2012).
- <sup>26</sup>L. M. Pham, N. Bar-Gill, D. Le Sage, C. Belthangady, A. Stacey, M. Markham, D. J. Twitchen, M. D. Lukin, and R. L. Walsworth, “Enhanced metrology using preferential orientation of nitrogen-vacancy centers in diamond”, *Physical Review B* **86**, 121202 (2012).
- <sup>27</sup>Y.-C. Chen, B. Griffiths, L. Weng, S. S. Nicley, S. N. Ishmael, Y. Lekhai, S. Johnson, C. J. Stephen, B. L. Green, G. W. Morley, M. E. Newton, M. J. Booth, P. S. Salter, and J. M. Smith, “Laser writing of individual nitrogen-vacancy defects in diamond with near-unity yield”, *Optica* **6**, 662–667 (2019).
- <sup>28</sup>E. E. Kleinsasser, M. M. Stanfield, J. K. Q. Banks, Z. Zhu, W.-D. Li, V. M. Acosta, H. Watanabe, K. M. Itoh, and K.-M. C. Fu, “High density nitrogen-vacancy sensing surface created via he+ ion implantation of 12c diamond”, *Applied Physics Letters* **108**, 202401 (2016).
- <sup>29</sup>K. Ohno, F. Joseph Heremans, L. C. Bassett, B. A. Myers, D. M. Toyli, A. C. Bleszynski Jayich, C. J. Palmstrøm, and D. D. Awschalom, “Engineering shallow spins in diamond with nitrogen delta-doping”, *Applied Physics Letters* **101**, 082413 (2012).
- <sup>30</sup>D. R. Glenn, D. B. Bucher, J. Lee, M. D. Lukin, H. Park, and R. L. Walsworth, “High-resolution magnetic resonance spectroscopy using a solid-state spin sensor”, *Nature* **555**, 351–354 (2018).

- <sup>31</sup>Davies G., Hamer M. F., and Price William Charles, “Optical studies of the 1.945 eV vibronic band in diamond”, *Proceedings of the Royal Society of London. A. Mathematical and Physical Sciences* **348**, 285–298 (1976).
- <sup>32</sup>N. B. Manson, J. P. Harrison, and M. J. Sellars, “Nitrogen-vacancy center in diamond: model of the electronic structure and associated dynamics”, *Physical Review B* **74**, 104303 (2006).
- <sup>33</sup>L. Robledo, H. Bernien, I. van Weperen, and R. Hanson, “Control and coherence of the optical transition of single nitrogen vacancy centers in diamond”, *Physical Review Letters* **105**, 177403 (2010).
- <sup>34</sup>L. Robledo, H. Bernien, T. v. d. Sar, and R. Hanson, “Spin dynamics in the optical cycle of single nitrogen-vacancy centres in diamond”, *New Journal of Physics* **13**, 025013 (2011).
- <sup>35</sup>A. Dréau, M. Lesik, L. Rondin, P. Spinicelli, O. Arcizet, J.-F. Roch, and V. Jacques, “Avoiding power broadening in optically detected magnetic resonance of single NV defects for enhanced dc magnetic field sensitivity”, *Physical Review B* **84**, 195204 (2011).
- <sup>36</sup>J. F. Barry, J. M. Schloss, E. Bauch, M. J. Turner, C. A. Hart, L. M. Pham, and R. L. Walsworth, “Sensitivity optimization for NV-diamond magnetometry”, arXiv:1903.08176 [cond-mat, physics:physics, physics:quant-ph] (2019).
- <sup>37</sup>S. Schäublin, A. Höhener, and R. Ernst, “Fourier spectroscopy of nonequilibrium states, application to CIDNP, overhauser experiments and relaxation time measurements”, *Journal of Magnetic Resonance* (1969) **13**, 196–216 (1974).
- <sup>38</sup>A. Jarmola, V. M. Acosta, K. Jensen, S. Chemerisov, and D. Budker, “Temperature- and magnetic-field-dependent longitudinal spin relaxation in nitrogen-vacancy ensembles in diamond”, *Physical Review Letters* **108**, 197601 (2012).
- <sup>39</sup>V. M. Acosta, E. Bauch, M. P. Ledbetter, A. Waxman, L.-S. Bouchard, and D. Budker, “Temperature dependence of the nitrogen-vacancy magnetic resonance in diamond”, *Physical Review Letters* **104**, 070801 (2010).
- <sup>40</sup>H. Demers, N. Poirier-Demers, A. R. Couture, D. Joly, M. Guilmain, N. de Jonge, and D. Drouin, “Three-dimensional electron microscopy simulation with the CASINO monte carlo software”, *Scanning* **33**, 135–146 (2011).
- <sup>41</sup>*ESTAR database.*

- <sup>42</sup>D. R. Glenn, R. R. Fu, P. Kehayias, D. L. Sage, E. A. Lima, B. P. Weiss, and R. L. Walsworth, “Micrometer-scale magnetic imaging of geological samples using a quantum diamond microscope”, *Geochemistry, Geophysics, Geosystems* **18**, 3254–3267 (2017).
- <sup>43</sup>V. V. Dremov, S. Y. Grebenchuk, A. G. Shishkin, D. S. Baranov, R. A. Hovhannisyan, O. V. Skryabina, N. Lebedev, I. A. Golovchanskiy, V. I. Chichkov, C. Brun, T. Cren, V. M. Krasnov, A. A. Golubov, D. Roditchev, and V. S. Stolyarov, “Local josephson vortex generation and manipulation with a magnetic force microscope”, *Nature Communications* **10**, 1–9 (2019).
- <sup>44</sup>T. Jungwirth, X. Marti, P. Wadley, and J. Wunderlich, “Antiferromagnetic spintronics”, *Nature Nanotechnology* **11**, 231–241 (2016).
- <sup>45</sup>D. R. Glenn, K. Lee, H. Park, R. Weissleder, A. Yacoby, M. D. Lukin, H. Lee, R. L. Walsworth, and C. B. Connolly, “Single cell magnetic imaging using a quantum diamond microscope”, *Nature methods* **12**, 736–738 (2015).
- <sup>46</sup>E. V. Levine, M. J. Turner, P. Kehayias, C. A. Hart, N. Langellier, R. Trubko, D. R. Glenn, R. R. Fu, and R. L. Walsworth, “Principles and techniques of the quantum diamond microscope”, *Nanophotonics* **8**, 1945–1973 (2019).
- <sup>47</sup>I. Fescenko, A. Laraoui, J. Smits, N. Mosavian, P. Kehayias, J. Seto, L. Bougas, A. Jarmola, and V. M. Acosta, “Diamond magnetic microscopy of malarial hemozoin nanocrystals”, *Physical Review Applied* **11**, 034029 (2019).
- <sup>48</sup>L. M. Coronado, C. T. Nadovich, and C. Spadafora, “Malarial hemozoin: from target to tool”, *Biochimica et Biophysica Acta (BBA) - General Subjects* **1840**, 2032–2041 (2014).
- <sup>49</sup>A. Butykai, A. Orbán, V. Kocsis, D. Szaller, S. Bordács, E. Tátrai-Szekeres, L. F. Kiss, A. Bóta, B. G. Vértessy, T. Zelles, and I. Kézsmárki, “Malaria pigment crystals as magnetic micro-rotors: key for high-sensitivity diagnosis”, *Scientific Reports* **3**, 1431 (2013).
- <sup>50</sup>L. M. Pham, S. J. DeVience, F. Casola, I. Lovchinsky, A. O. Sushkov, E. Bersin, J. Lee, E. Urbach, P. Cappellaro, H. Park, A. Yacoby, M. Lukin, and R. L. Walsworth, “NMR technique for determining the depth of shallow nitrogen-vacancy centers in diamond”, *Physical Review B* **93**, 045425 (2016).

- <sup>51</sup>S. J. DeVience, L. M. Pham, I. Lovchinsky, A. O. Sushkov, N. Bar-Gill, C. Belthangady, F. Casola, M. Corbett, H. Zhang, M. Lukin, H. Park, A. Yacoby, and R. L. Walsworth, “Nanoscale NMR spectroscopy and imaging of multiple nuclear species”, *Nature Nanotechnology* **10**, 129–134 (2015).
- <sup>52</sup>N. Aslam, M. Pfender, P. Neumann, R. Reuter, A. Zappe, F. F. d. Oliveira, A. Denisenko, H. Sumiya, S. Onoda, J. Isoya, and J. Wrachtrup, “Nanoscale nuclear magnetic resonance with chemical resolution”, *Science* **357**, 67–71 (2017).
- <sup>53</sup>H. J. Hogben, M. Krzystyniak, G. T. P. Charnock, P. J. Hore, and I. Kuprov, “Spinach—a software library for simulation of spin dynamics in large spin systems”, *Journal of Magnetic Resonance* (San Diego, Calif.: 1997) **208**, 179–194 (2011).